Low Temperature Physics/Fizika Nizkikh Temperatur, 2012, v. 38, No. 1, p. 52–61

# Magnetic proximity effect in $Pr_{0.5}Ca_{0.5}MnO_3/La_{0.7}Sr_{0.3}MnO_3$ bilayered films

V.G. Prokhorov, G.G. Kaminsky, and V.S. Flis

*Institute of Metal Physics of National Academy of Sciences of Ukraine, Kiev 03142, Ukraine*
E-mail: pvg@imp.kiev.ua

J.M. Kim, T.W. Eom, J.S. Park, and Y.P. Lee

*q-Psi and Department of Physics, Hanyang University, Seoul 133-791, Korea*

V.L. Svetchnikov

*National Center for HREM, TU Delft 2628AL, The Netherlands*

Received January 27, 2011, revised April 18, 2011

The magnetotransport properties of $Pr_{0.5}Ca_{0.5}MnO_3/La_{0.7}Sr_{0.3}MnO_3$ bilayer, and $Pr_{0.5}Ca_{0.5}MnO_3$ and $La_{0.7}Sr_{0.3}MnO_3$ films, deposited on $LaAlO_3$ (001) substrate by pulse laser deposition have been investigated. The x-ray diffraction and high-resolution electron-microscopy analysis reveals that lattice parameters for the constituent sublayers in the bilayer are very close to that for the individual films. It was found that a ferromagnetic transition in the $La_{0.7}Sr_{0.3}MnO_3$ sublayer significantly modifies the magnetotransport properties of the $Pr_{0.5}Ca_{0.5}MnO_3$ constituent sublayer, owing to occurrence of a *magnetic proximity effect*. The main evidences for this effect are an appearance of the exchange bias interaction between the constituent sublayers; a localized-to-itinerant crossover in the system of polarized electrons, which results in formation of the Griffiths-like ferromagnetic state; and an unusual polaron transport of carriers. The experimental results have been analyzed within the framework of modern theoretical approaches.

PACS: **71.30.+h** Metal-insulator transitions and other electronic transitions;
75.47.Lx Magnetic oxides;
**75.70.–i** Magnetic properties of thin films, surfaces, and interfaces.

Keywords: magnetotransport properties, ferromagnetic transition, magnetic proximity effect.

## 1. Introduction

The combination of ferromagnetic (FM) and antiferromagnetic (AFM) layers have attracted considerable attention due to their interesting fundamental science and potential for applications as magnetic metamaterials with desired magnetic properties. On the other hand, the development of hybrid devices based on multilayered films needs detailed information on the mutual influence between constituent layers. This influence is generally referred to as a *magnetic proximity effect* [1], similar to a well-known *proximity effect*, which is typical for superconductors. One of a principal effect provided by the magnetic coupling between the FM and the AFM layers is manifested by a shift of the hysteresis loop along the field axis of a ferromagnet, and is termed as the exchange bias interaction [2,3]. At the same time the mutual influence between adjacent FM/AFM layers can significantly modify a thermodynamic behavior of these objects in the wide temperature range [4]. Furthermore, a *magnetic proximity effect* can occur due to the interaction between two magnetic layers with different FM spin-ordering temperatures ($T_C$). The layer with the higher ordering temperature induces magnetic order into the layer with the lower ordering temperature at temperatures at which the latter would be paramagnetic. Similar effects were observed in bilayered and multilayered manganite films which manifest not only a significant enhancement of the ferromagnetic ordering in the low-$T_C$ layers, but show the anisotropy of saturation magnetization and the alternating shape of the temperature-dependent anisotropic magnetoresistance near the metal–insulator transition [5–9]. In spite of that a *magnetic proximity effect* have already been studied for a long time, the physical nature is still poorly understood.

In this paper, we report the experimental results for the $Pr_{0.5}Ca_{0.5}MnO_3/La_{0.7}Sr_{0.3}MnO_3$ bilayer (BL) and the pure $Pr_{0.5}Ca_{0.5}MnO_3$ (PCMO) film, emphasizing a significant modification in magnetic behavior for the PCMO sublayer, stimulated by a *magnetic proximity effect*.

## 2. Experimental techniques

A cross-beam laser-ablation technique was employed for the preparation of the films [10]. We used two Nd-YAG lasers with a wavelength of 1064 nm, a pulse duration of 7.8–10.5 ns, a pulse-repetition rate of 20 Hz, and an energy of 0.3 J/pulse. The power density of laser beam focused on the target was $9.5\cdot10^8$–$2\cdot10^{10}$ W/cm$^2$. The targets were manufactured from the PCMO and LSMO powders of the stoichiometric composition by hot-pressing and heating at 1200 °C for 4 days in air. The oxygen pressure in chamber was 200 Torr during deposition and 600 Torr during cooling. All films were deposited on a $LaAlO_3$ (001) single crystal (LAO) with a thickness of $\simeq$ 300 nm at the substrate temperature of 770 °C. The thickness of sublayers in BL was 150 nm with PCMO at the top. Only the as-deposited films were used for measurements.

The θ–2θ x-ray diffraction (XRD) patterns were obtained using a Rigaku diffractometer with Cu $K_\alpha$ radiation. The lattice parameters evaluated directly from the XRD data were plotted against $\cos^2\theta/\sin\theta$. With an extrapolated straight line to $\cos^2\theta/\sin\theta = 0$, a more precise lattice parameter was obtained. The high-resolution electron-microscopy (HREM) studies were carried out by using a Philips CM300UT-FEG microscope with a field emission gun operated at 300 kV. The point resolution of the microscope was in the order of 0.12 nm. The cross-sectional specimens were prepared by the standard techniques using mechanical polishing followed by ion-beam milling at a grazing incidence. The microstructure analysis was carried out at room temperature. The in-plane field-cooled (FC) and zero-field-cooled (ZFC) magnetization curves were performed by using a Quantum Design SQUID magnetometer. To avoid an influence of the parasitic (manly diamagnetic) response from LAO, the magnetization curves obtained for the bare substrates were extracted from the raw experimental curves. The resistance measurements were performed by using the four-probe method in a temperature range of 10–300 K and in a magnetic field up to 5 T.

## 3. Microstructure

Figure 1 shows the cross-sectional HREM image for BL which manifests the well-defined sharp interface between sublayers. Inset (*a*) presents the θ–2θ XRD scans for PCMO, LSMO and BL. High intensities of the (002) peaks manifest that the deposition results in highly *c*-oriented films. The Bragg peak for BL displays a double-peak peculiarity, which can be considered as a presence of two crystalline phases, belonging to the LSMO and PCMO sublayers,

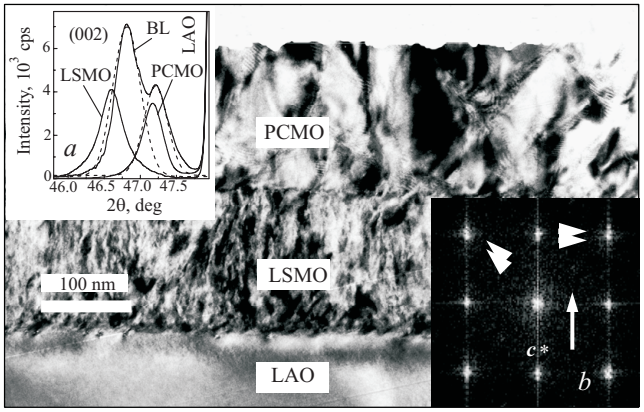


*Fig. 1.* Low-magnification cross-sectional HREM image for the PCMO/LSMO bilayer. The (002) Bragg peaks for the PCMO and LSMO film, and the PCMO/LSMO bilayer (*a*). The FFT pattern for the PCMO/LSMO interface (*b*).

and can be fitted by two Lorenz functions (dashed lines). Analysis of the XRD data reveals that the out-of-plane lattice parameter is $c \simeq$ 0.384 and 0.389 nm for PCMO and LSMO, respectively, while $c \simeq$ 0.3867 and 0.3874 nm for the corresponding sublayers in BL. Inset (*b*) displays the fast Fourier transform (FFT) of the high-magnification cross-sectional HREM image for the BL region, including the interface between sublayers. The slight splitting of fundamental Bragg spots (indicated by white arrows) confirms a difference of crystal lattice for the constituent sublayers that is coincident with the XRD data. Analyzing the interspot spacings on the FFT patterns and the HREM images the following lattice parameters (for pseudocubic symmetry) were obtained: $a = b \simeq$ 0.3841 and 0.386 nm; $c/a \simeq$ $\simeq$ 1.0076 and 1.0078 for PCMO and LSMO, respectively, while $a = b \simeq$ 0.3842 and 0.3861 nm; $c/a \simeq$ 1.0065 and 1.0068 for the corresponding sublayers in BL. Here $a$ and $b$ are the in-plane lattice parameters. It is clear that the cross-sectional HREM analysis can not distinguish difference between $a$ and $b$. In spite of that the obtained results are well coincident with those for the bulk compounds [11,12].

Therefore, the lattice parameters for the constituent sublayers in BL are very close to that for the individual films. Moreover, the tetragonal ratio, $c/a$, which defines a lattice distortion, provided by a lattice strain, is also almost the same for the individual films and the BL's sublayers.

## 4. Experimental results

Figure 2 displays the temperature dependences of the in-plane FC and ZFC magnetic moment, $M(T)$, for the PCMO film measured at different applied magnetic fields, $H$. The experimental curves testify that the film undergoes two magnetic transitions with a decreasing temperature. There are a broad and smooth magnetic transition at $T_{C,N} \lesssim$ 150 K, which is typical for this compound [13], and the next one at $T^* \lesssim$ 50 K, which is manifested by a

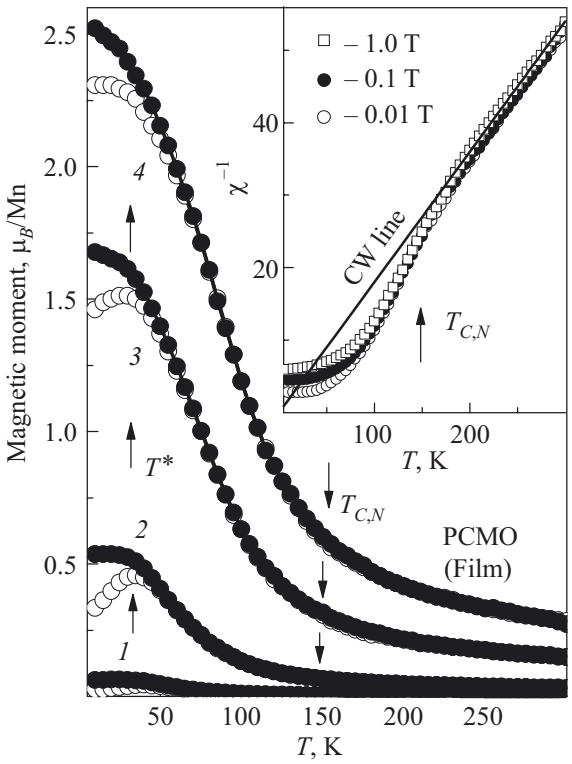


*Fig. 2.* Temperature dependences of the in-plane FC (solid symbols) and ZFC (open symbols) magnetic moment for the PCMO film measured at $H$, T: 0.01 (*1*), 0.1 (*2*), 0.5 (*3*), and 1 (*4*). The inset presents the temperature dependences of the inverse dc susceptibility for the same film. The solid line is the linear fit within the Curie–Weiss model.

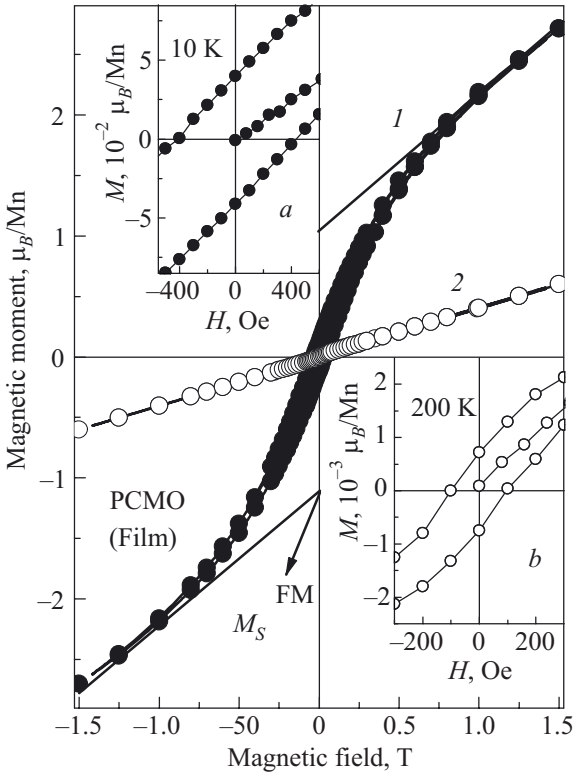


*Fig. 3.* The in-plane hysteresis loops for the PCMO film measured at $T$, K: 10 (*1*) and 200 (*2*). Straight lines are the linear extrapolation of the AFM term. The insets shows the same curves in detail. Lines are a guide to the eyes.

splitting of FC/ZFC $M(T)$, curves. First of them, according to the magnetic phase diagram [13], is connected with a transition from the paramagnetic (PM) to the AFM (or mixed AFM/FM) phase with the decreasing temperature. More exactly the $T_{C,N}$ value can be determined from the temperature dependence of the inverse dc susceptibility, $\chi^{-1}(T)$, represented by the inset, at a point where the $\chi^{-1}(T)$ curve starts to be deviated from the Curie–Weiss linear behavior (straight line), which is typical for a paramagnet. Here $\chi = M / \mu_0 H$ is a dimensionless value, where $\mu_0 = 4\pi \cdot 10^{-7}$ H/m is a permeability. Second magnetic transition is very often observed in the manganite compounds and is interpreted as an appearance of the spin-glass-like (or cluster-glass) state originated from a phase-separation effect [13,14].

Figure 3 presents the in-plane hysteresis loops, $M(H)$, for the PCMO film taken at different temperatures. The $M(H)$ dependence at 10 K (curve *1*, solid symbols) can be treated as a superposition of the AFM (linear term) and the FM [hysteresis term, represented by the inset (*a*)] contributions. The linear extrapolation of a high-field $M(H)$ behavior to $H = 0$ (indicated by straight lines) allows us to obtain a saturation magnetic moment for the FM phase which turn out to be $M_s^{FM} \simeq 1.0\ \mu_B$ / Mn at 10 K. There are a coercive field $H_c \simeq \pm$ 320 Oe and a remanent magnetic moment $M_r \simeq \pm\ 0.12\ \mu_B$ / Mn. Therefore, the magnetic transition at $T_{C,N} \simeq$ 150 K can be treated as a multiphase transformation with a formation of the AFM and FM phases simultaneously. Inset (*b*) shows that the hysteresis behavior of the magnetization loop, typical for the FM phase, still persists at $T =$ 200 K, where the film should be in the PM state. At this temperature ($T = 200$ K $> T_{C,N}$) the following magnetic characteristics were obtained: $M_s^{FM} \simeq 0.015\ \mu_B$ / Mn, $H_c \simeq \pm$ 100 Oe and $M_r \simeq \pm\ 0.0002\ \mu_B$ / Mn.

Figure 4 displays the temperature dependences of the in-plane FC and ZFC magnetic moment, $M(T)$, for BL measured at different applied magnetic fields. For comparison the inset shows the same dependences for the LSMO film. It is seen that BL undergoes three magnetic transitions with the decreasing temperature. First of them occurs at $T_C \simeq$ 325 K and manifests the PM $\rightarrow$ FM transition in the LSMO sublayer. It is confirmed by the same value of the Curie temperature observed for the LSMO individual film (see inset). Second one at $T_{C,N}$ belongs to the PCMO sublayer and is connected with a composite AFM/FM transition. Similar to the PCMO individual film, BL demonstrates a well-defined ZFC/FC $M(T)$ splitting at low temperature. Because this phenomenon does not observe for the LSMO individual film (see inset), one can conclude that the magnetic transition at $T^*$ belongs to the PCMO sublayer only.

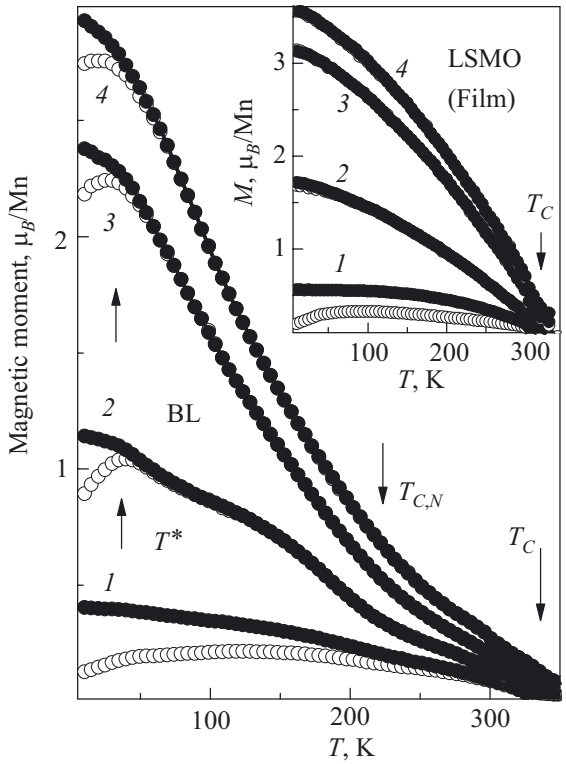


*Fig. 4*. Temperature dependences of the in-plane FC (solid symbols) and ZFC (open symbols) magnetic moment for the PCMO/LSMO bilayer measured at *H*, T: 0.01 (*1*), 0.1 (*2*), 0.5 (*3*), and 1 (*4*). The inset presents the same dependences for the LSMO film. Lines are a guide to the eyes.

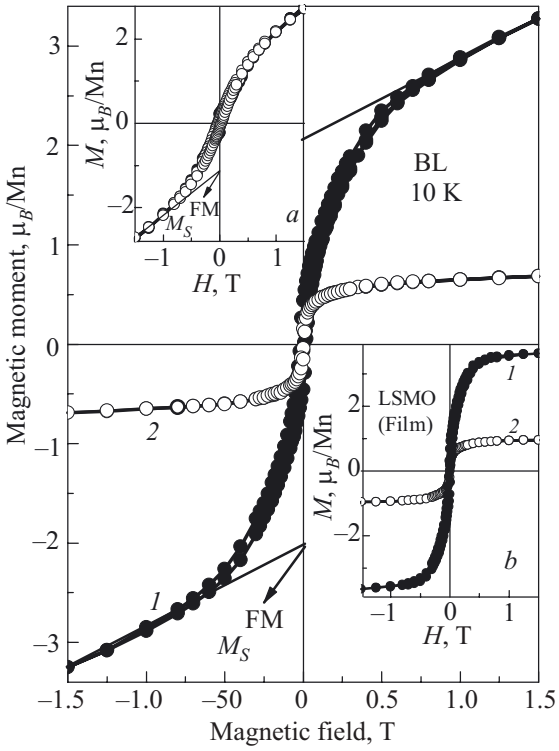


*Fig. 5*. The in-plane hysteresis loops for the PCMO/LSMO bilayer measured at *T*, K: 10 (*1*) and 200 (*2*). Lines are a guide to the eyes. Straight lines are the linear extrapolation of the AFM term. The inset (*a*) presents the hysteresis loop for the PCMO film (solid symbols) and the PCMO sublayer (open symbols), extracted from the total $M(T)$ for the PCMO/LSMO bilayer (see text). The inset (*b*) shows the hysteresis loops for the LSMO film taken at *T*, K: 10 (*1*) and 200 K (*2*).

Figure 5 presents the in-plane hysteresis loops, $M(H)$, for BL taken at different temperatures. Similar to the PCMO film the $M(H)$ dependence at 10 K (curve *1*, solid symbols) also can be treated as a superposition of the AFM (linear term) and the FM (hysteresis term with the saturation magnetic moment) contributions. Analysis of the $M(H)$ behavior reveals that $M_s^{FM} \simeq 2.1\ \mu_B$/Mn, $H_c \simeq \pm 180$ Oe and $M_r \simeq \pm 0.45\ \mu_B$/Mn for BL at 10 K. At the same time the $M(H)$ curve at 200 K demonstrates behavior typical for a FM phase with the saturation magnetic moment of $M_s^{FM} \simeq 0.565\ \mu_B$/Mn and the $M(H)$ hysteresis of $H_c \simeq \pm 54$ Oe and $M_r \simeq \pm$ $\pm 0.154\ \mu_B$/Mn. Analysis of the corresponding hysteresis loops for LSMO, represented by the inset (*b*), reveals that $M_s^{FM} \simeq 3.43$ and 1.15 $\mu_B$/Mn, $H_c \simeq \pm 165$ and 53 Oe, $M_r \simeq \pm 0.7$ and 0.197 $\mu_B$/Mn at $T = 10$ and 200 K, respectively. At 10 K a saturation magnetic moment of the FM phase for BL is almost equal to a half-sum of the corresponding magnitudes for the PCMO and LSMO individual films: $M_s^{FM}$ (BL) $\simeq [M_s^{FM}$ (PCMO) + $+ M_s^{FM}$ (LSMO)]/2. Such summation is correct because thickness of the individual sublayers in BL is twice smaller than that for the individual films. At the same time $M_s^{FM}$ (BL) $\simeq M_s^{FM}$ (LSMO)/2 at 200 K, manifesting that a major part of the FM phase belongs to the LSMO sublayer while the basic state for the PCMO sublayer is close to PM. For comparison the inset (*a*) displays the experimental hysteresis loop for the PCMO film (solid symbols) and the PCMO sublayer (open symbols), which was extracted from the total $M(H)$ curve for BL by a following procedure: $M_{\text{extr}}^{PCMO}(H) = 2\times[M^{BL}(H) - M^{LSMO}(H)/2]$, where $M^{BL}(H)$ and $M^{LSMO}(H)$ are the experimental $M(H)$ curves for BL and LSMO, respectively, at 10 K. It is seen that both dependencies are almost exactly coincident and have the same $M_s^{FM}$, $H_c$ and $M_r$ values. Therefore, one can conclude that the shape of hysteresis loop for BL is controlled mainly by a magnetic behavior of the constituent sublayers and can be constructed by a direct summation of the $M(H)$ curves for the individual films. It is worth noting that the considered hysteresis loops were measured after cooling without an applied magnetic field (ZFC regime).

Figure 6 presents the in-plane hysteresis loops, $M(H)$, for BL taken at 10 K, which were measured after cooling without (solid symbols) and with (open symbols) an applied magnetic field of 0.5 T. Insets show that the hysteresis loop of BL after cooling with an applied magnetic

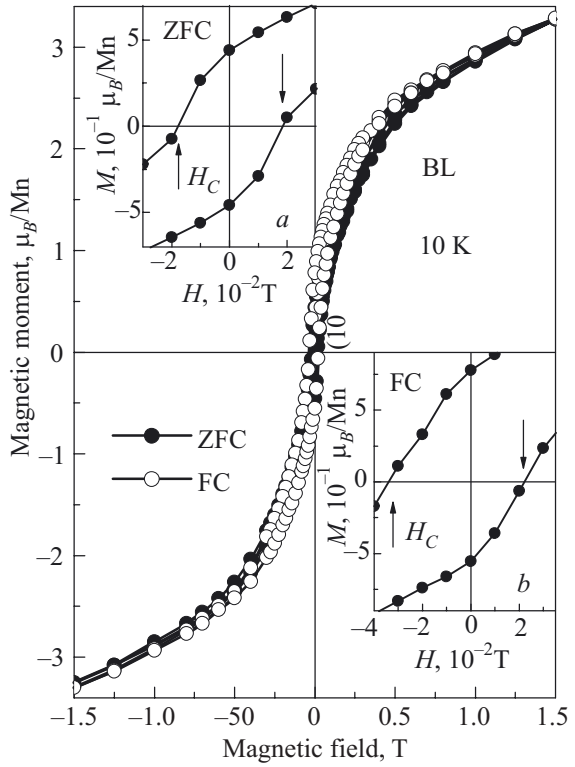


*Fig. 6*. The in-plane hysteresis loops for the PCMO/LSMO bilayer at $T$ = 10 K measured after the cooling without (ZFC regime, solid symbols) and with (FC regime, open symbols) an applied magnetic field of 0.5 T. The insets (*a*) and (*b*) present the same curves in detail. Lines are a guide to the eyes. The asymmetric shape of the hysteresis loop, represented by the inset (*b*) testifies an appearance of the exchange bias interaction.

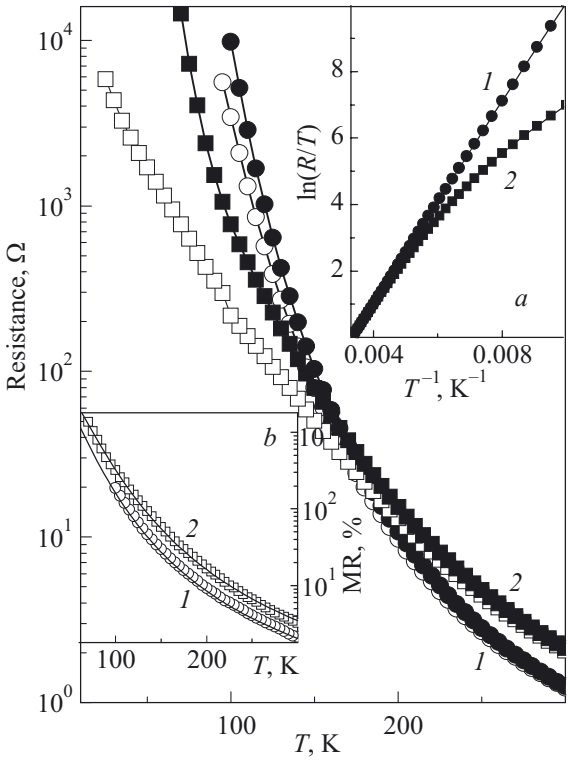


*Fig. 7*. Temperature dependences of the resistance for the PCMO film (*1*) and the PCMO/LSMO bilayer (*2*) measured without (solid symbols) and with (open symbols) an applied magnetic field of 5 T. Lines are a guide to the eyes. The inset (*a*) presents the $\ln(R/T) - \text{vs} - T^{-1}$ plot for the same samples without an applied magnetic field. Lines are a guide to the eyes. The inset (*b*) displays the temperature-dependent MR ratio for the same samples. The solid lines are the theoretical curves obtained within the framework of the magnetic polaron model.

field (FC regime) becomes asymmetric: $H_c \simeq -338$ and + 224 Oe [see inset (*b*)]. A shift of the hysteresis loop along the field axis is observed, as a rule, for the FM/AFM magnetically coupled system and is called the "exchange bias" (EB) interaction. The EB, resulting from the exchange anisotropy at the FM/AFM interface, is provided by the coupling between the FM layer and the uncompensated interfacial spins in the AFM layer, the number of which determines the magnitude of exchange field ($H_{EB}$) [2,3]. This effect is observed upon cooling the FM/AFM bilayer in the presence of a static magnetic field from a temperature above the Néel point but below the Curie one down to a certain temperature $T < T_N$. In our case the FM LSMO sublayer has $T_C \simeq$ 325 K while the AFM/FM PCMO one has $T_N \simeq$ 150 K. Therefore, cooling down BL upon an applied magnetic field from a room temperature up to 10 K, we realize a necessary condition for an appearance of the EB interaction. Moreover, the average coercive field, $\langle H_c \rangle \simeq$ 281 Oe, becomes larger after cooling in the FC regime, than that for the ZFC one, $H_c \simeq \pm$ 180 Oe (see inset (*a*)) that also is typical for the EB effect [2,3].

Figure 7 is the temperature-dependent resistance, $R(T)$, for PCMO (*1*) and BL (*2*) without (solid symbols) and with (open symbols) an applied magnetic field of 5 T. The magnetic field and the transport current were parallel to the film surface. Because PCMO is a top sublayer of BL, which remains insulating at all temperatures, and the electrical contacts are placed onto its surface, one can conclude that the obtained $R(T)$ dependence belongs to the PCMO sublayer only. In other words, the parallel-resistor circuit (with the low-resistance FM LSMO sublayer as a shunt) can not be realized in this case. Both PCMO (*1*) and BL (*2*) demonstrate close to exponential rise of resistance with the decreasing temperature without the metal–insulator (MI) transition in the whole temperature interval. On the other hand, a more detail analysis reveals a significant difference in the $R(T)$ behavior for the PCMO film and the PCMO sublayer. Inset (a) displays the $\ln(R/T) - \text{vs} - T^{-1}$ plot for the same samples which exhibits a straight-line-like dependence for PCMO while a nonlinear behavior in the whole temperature interval for the PCMO sublayer. Moreover, any peculiarities, connected with a formation of the CO state (as a sharp

change in the slope of these curves, for example), did not found. It can be explained by influence of the lattice strain which leads to suppression of the CO ordering, because the as-deposited films were used for these measurements [10–18], or to significant increase of the CO temperature higher than a room one [19]. Inset (*b*) shows that the magnetoresistance (MR) value is higher for the PCMO sublayer than that for the PCMO film at all temperatures. Here MR is defined by $100\% \times [R(0) - R(H)] / R(H)$, where $R(0)$ and $R(H)$ are the resistances without and with an applied magnetic field of 5 T.

### 5. Discussion

Let us analyze the obtained results in terms of a magnetic proximity effect or a magnetic coupling between the constituent layers in BL. As is evident from the foregoing the hysteresis loops are almost the same for the PCMO individual film and the PCMO sublayer, grown on LSMO, (see inset (*a*) in Fig. 5) that testify a very insignificant mutual influence between the BL's sublayers. However, the cooling of BL under an applied magnetic field (FC regime) leads to an appearance of the EB interaction, which is manifested by a shift of the hysteresis loop along a magnetic field axis. This phenomenon can be treated as an evidence for a magnetic proximity effect in the PCMO/LSMO bilayer.

Now we will consider the magnetic influence of the FM LSMO sublayer on the thermodynamic characteristics of the PCMO one, such as the $M(T)$ dependencies taken at different magnetic fields. Similar to a hysteresis loop (see Fig. 5) the $M(T)$ curves for the PCMO sublayer were extracted from the total $M(T)$ dependencies for BL: $M_{\text{extr}}^{PCMO}(T) = 2 \times [M^{BL}(T) - M^{LSMO}(T) / 2]$, where $M^{BL}(T)$ and $M^{LSMO}(T)$ are the experimental $M(T)$ curves for BL and LSMO, respectively.

Figure 8 presents the in-plane ZFC (open symbols) and FC (solid symbols) $M(T)$ dependences for the PMCO sublayer (square symbols) measured at different magnetic field. For comparison the same dependences for the PCMO individual film (circle symbols) are shown as well. It is seen that the PCMO sublayer manifests the $M(T)$ behavior at $H =$ 0.01 T, which is typical for the FM phase with the Curie point close to that for the LSMO sublayer. At the same time the FM state is drastically suppressed with the increasing external magnetic field and becomes almost undistinguished at $H =$ 1 T. In the last case the $M(T)$ curves for the PCMO film and the PCMO sublayer are almost coincident. More clearly it can be observed on the temperature dependences of the inverse dc susceptibility, represented by Fig. 9. Inset shows that $\chi^{-1}(T)$ dependence, taken at $H =$ 0.01 T, excellently described by the Bloch law $\sim (T_C - T)^{-3/2}$, with $T_C =$ 330 K (solid line), which is typical for common FMs [20]. On the other hand, $\chi^{-1}(T) \sim (T - \theta)$ at $H =$ 1 T (straight line, curve *3*), manifesting the occurrence of the PM state, where $\theta$ is a characteristic temperature. A frustration of the long-range spin ordering by an applied magnetic field (that is not typical for common FMs) allow us to suggest that the observed FM state has a fluctuation origin. The long-term spin-ordered fluctuations can appear in the PM matrix, leading to the formation of the Griffiths phase [21] above the FM transition point ($T > T_{C,N} \simeq$ 150 K). Moreover, at $H \to 0$ these fluctuations can coalesce and result in the formation of the large-size FM clusters [22], which are observed in our case at $H =$ 0.01 T (see Figs. 8, 9). According to theoretical prediction the Griffiths phase is suppressed by an applied magnetic field that also correlates with our results. The observed broad peak on the ZFC and FC $M(T)$ curves for the PCMO sublayer near $T_{C,N}$ at $H =$ 0.1 T testifies that the Griffiths-like fluctuations become more stable in a region of the magnetic phase transition, that is typical for such type of the formations. It is explained by an unlimited rise of the correlation length at a

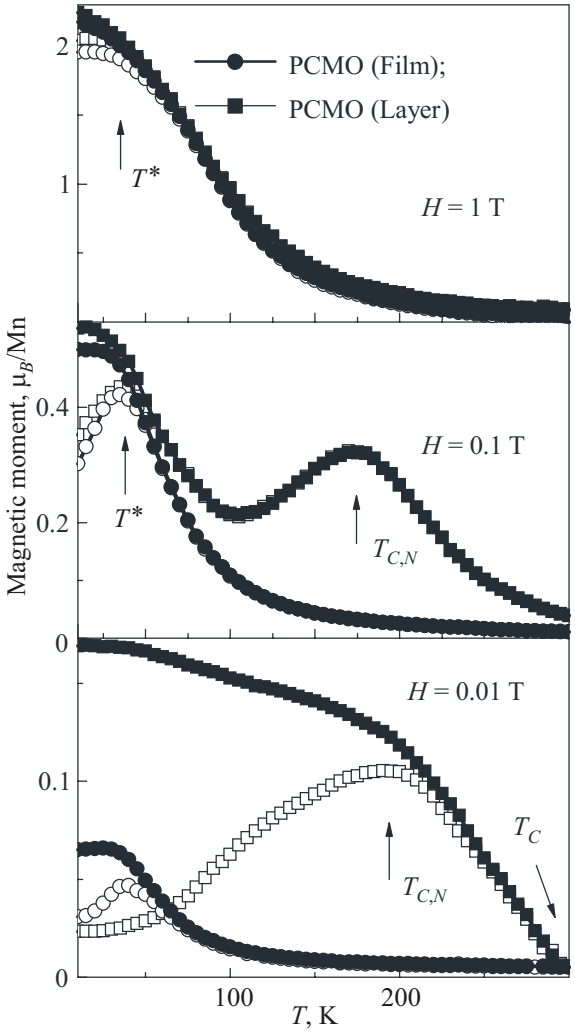


*Fig. 8.* Temperature dependences of the in-plane FC (solid symbols) and the ZFC (open symbols) magnetic moment for the PCMO film (circle symbols) and the PCMO sublayer (square symbols) taken at a different applied magnetic field.

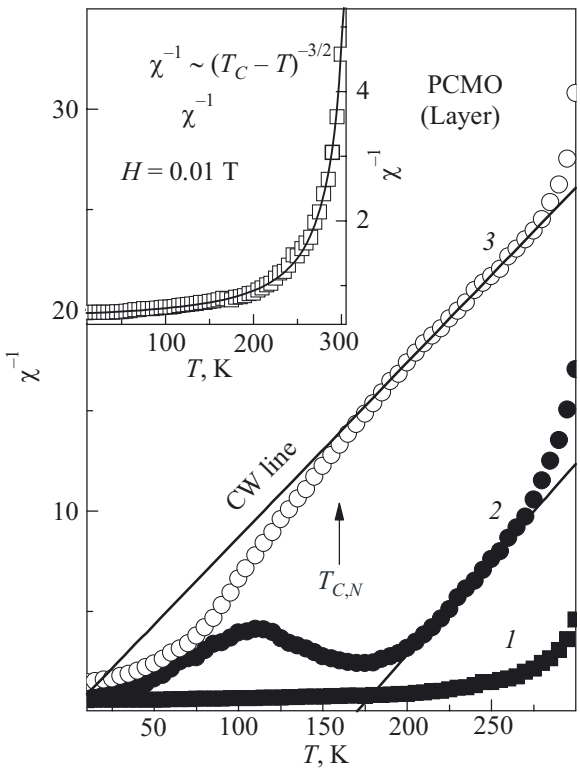


*Fig. 9*. Temperature dependences of the inverse dc susceptibility $\chi^{-1}$ for the PCMO sublayer measured at $H$, T: 0.01 (*1*), 0.1 (*2*), and 1 (*3*). The solid lines are the linear fit within the Curie–Weiss model. The inset shows the same curve at $H$ = 0.01 T. The solid line is the Bloch's curve for the FM state.

critical point of the magnetic transition. Consequently, one can conclude that the FM LSMO sublayer induces a magnetic order into the PCMO sublayer, which is resulted in an appearance of the Griffiths-like state at temperature at which the PCMO sublayer would be paramagnetic.

The inset in Fig. 2 and Fig. 9 exhibit the linear $\chi^{-1}(T)$ behavior at $T \geq T_{C,N}$ for the PCMO film and the PCMO sublayer, respectively. In the latter case it is true at high magnetic field only. Such type of dependence is typical for the PM materials [23] and can be expressed by the Curie–Weiss (CW)-type law: $\chi^{-1}(T) \sim (T + \theta)/C_{CW}$, where $C_{CW} = N\mu_{\text{eff}}^2 / 3k_B$ is the CW constant, which can be obtained from the experimental curve, $\mu_{\text{eff}}$ is the atom's effective magnetic moment, and $N$ is the number of atoms per unit cell. Analysis reveals that effective magnetic moment, obtained from the experimental data, $\mu_{\text{eff}} \simeq$ 13.3 and 17.8 $\mu_B$ for the PCMO film and the PCMO sublayer, respectively, is larger than that is predicted by the CW-theory for a classical PM, $\mu_{\text{eff}}^{\text{theor}} \simeq 4.42\ \mu_B$/Mn. The following expression was used for its estimation:

$$\mu_{\text{eff}}^{\text{theor}} = g\sqrt{xS_1(S_1+1)+(1-x)S_2(S_2+1)},$$

where, $g = 2$ is the Landé factor, $x$ is the Ca concentration, and $S_1 = 3/2$ and $S_2 = 2$ are the spin values of $Mn^{4+}$ and $Mn^{+3}$ ions, respectively. A similar PM response with the enhanced magnetic moment has already been observed in the manganites [24] and was attributed to an existence of the magnetic small-size polarons, which are typical for the diluted magnetic semiconductors. In this case the expression for the effective magnetic moment can be modified:

$$\mu_{\text{eff}}^{\text{theor}} =$$

$$= g\sqrt{x(S_1+S_2P)(S_1+S_2P+1)+(1-x-Px)S_2(S_2+1)},$$

where $0 \leq P \leq 6$ is a number of the polarized electrons [25]. The carried out calculations reveal that $P \simeq$ 4.2 and 5.8 for the PCMO film and the PCMO sublayer, respectively, which are well coincident with the theoretical prediction [25]. Taking into account the experimental $\mu_{\text{eff}}$ values and assuming a spherical shape of the magnetic polarons with a volume of $\pi D^3/6$, we estimate their average diameter to be $D \simeq$ 0.75 and 0.79 nm for the PCMO film and the PCMO sublayer, respectively. It is worth noting that the magnetic polaron clusters of the similar size origin have already observed in the PCMO compound by a neutron scattering [26], a magnetic measurement [27], and an electron-microscopy study [28]. Therefore, the FM LSMO sublayer introduces the magnetic order into the PCMO sublayer and gives an impetus to a topological magnetic transformation from the small-size magnetic-polaron-PM state to the Griffiths-like phase with the large-size fluctuated FM clusters. In other words it is the localized-to-itinerant crossover in the system of electrons [14].

Let us consider the transport properties of the PCMO film and the PCMO sublayer, taking into account the presence of the magnetic polarons. Inset (a) in Fig. 7 manifests that the $\ln(R/T) - \text{vs} - T^{-1}$ dependence is linear for the PCMO film while significantly deviated from that for the PCMO sublayer. Traditionally, the thermally-activated polaronic transport of carriers in the manganites expressed by $R(T,H) = R_0 T \exp(E_a/k_B T)$ [29]. Here $R_0$ is the constant, which is inversely proportional to the polaron hopping frequency, $E_a$ is the activation energy, and $k_B$ is the Boltzmann constant. However, the interaction between the auto-localized electron and the surrounding spins leads to a modification of the activation energy [30,31]. In this case the activation energy has to change in the presence of a spin-ordered coating, $E_a = E_a^0(1 - \langle\cos\theta_{ij}\rangle)$, where $E_a^0$ is the field-independent activation energy and $\theta_{ij}$ is the angle between the $i$ and $j$ ion spins. Taking into account, that for the uncorrelated spins $\langle\cos\theta_{ij}\rangle = \langle\cos\theta_i\rangle^2 = (M/M_s)^2$, one can to write $E_a = E_a^0[1-(M/M_s)^2]$, where $M_s$ is a saturation magnetic moment. For convenience will be used an expression for the temperature-dependent magnetic moment of the magnetic polaron $M(T,H) = M(0,H)\exp(-k_B T/\mu_{\text{eff}} H)$, where $M(0,H)$ is the

magnetic moment at $T = 0$ and $\mu_{\text{eff}}$ is the effective magnetic moment of magnetic polaron cluster [32]. Therefore, the $R(T,H)$ dependence for a magnetic polaron can be written as

$$R(T,H) = R_0 T \exp\left\{\frac{E_a^0\left[1-\exp\left(-k_B T/\mu_{\text{eff}}H\right)^2\right]}{k_B T}\right\}. \quad (1)$$

The experimental $\ln(R/T) - \text{vs} - T^{-1}$ curves for the PCMO film can be excellently described by the presented expression (solid lines) with the fitting parameters of $E_a^0 \simeq 1500$ K ($H = 0$), and $E_a^0 \simeq 1500$ K and $\mu_{\text{eff}} \simeq 20$ $\mu_B$ ($H = 5$ T) (see Fig. 10,*a*). In contrast to that the PCMO sublayer manifests the nonlinear $\ln(R/T) - \text{vs} - T^{-1}$ behavior even though an applied magnetic field is absent. It can be explained by the following reasons. First, the internal magnetic field in BL can be originated from the spontaneous magnetization of the LSMO sublayer, which has Curie point $T_C \simeq 325$ K. Analysis of the magnetic properties for BL (a remanent magnetic moment, for example) reveals that the FM transition in the LSMO sublayer results in the occurring magnetic field of about 0.01 T onto its surface. It is coincident with the published data on a spontaneous magnetization for the single-crystalline $La_{0.7}(Sr,Ca)_{0.3}MnO_3$ film [33]. Second, the analysis of the $M(T)$ curves for the PCMO sublayer (see Fig. 8) reveals that due to a *magnetic proximity* effect the large-size FM clusters are formed at $H \to 0$. Using $H = 0.01$ and 5 T, and $E_a^0 \simeq 1500$ K, the experimental $\ln(R/T) - \text{vs} - T^{-1}$ curves for the PCMO sublayer were fitted on the base of Eq. (1) with $\mu_{\text{eff}}$ as a fitting parameter. Without an applied magnetic field the better agreement between the experimental and theoretical curves observed for $\mu_{\text{eff}} \simeq 20\,000\,\mu_B$ while at $H = 5$ T the effective magnetic moment becomes significantly smaller, $\mu_{\text{eff}} \simeq 40\,\mu_B$. The obtained results are completely correlated with the magnetization data and testify that the giant FM clusters occur at $H \to 0$, which size is crucial decreased by an applied magnetic field. The solid lines shown by the inset (*b*) in Fig. 7 demonstrate that the MR($T$) dependences taken at $H = 5$ T also can be excellently described on the base of magnetic polaron model with the same fitting parameters: $E_a^0 \simeq 1500$ K, and $\mu_{\text{eff}} \simeq 20\,\mu_B$ and $40\,\mu_B$ for the PCMO film and the PCMO sublayer, respectively. Therefore, a magnetic proximity effect manifests itself in the transport properties of the PCMO/LSMO bilayer as a nonlinear $\ln(R/T) - \text{vs} - T^{-1}$ dependence without an applied magnetic field.

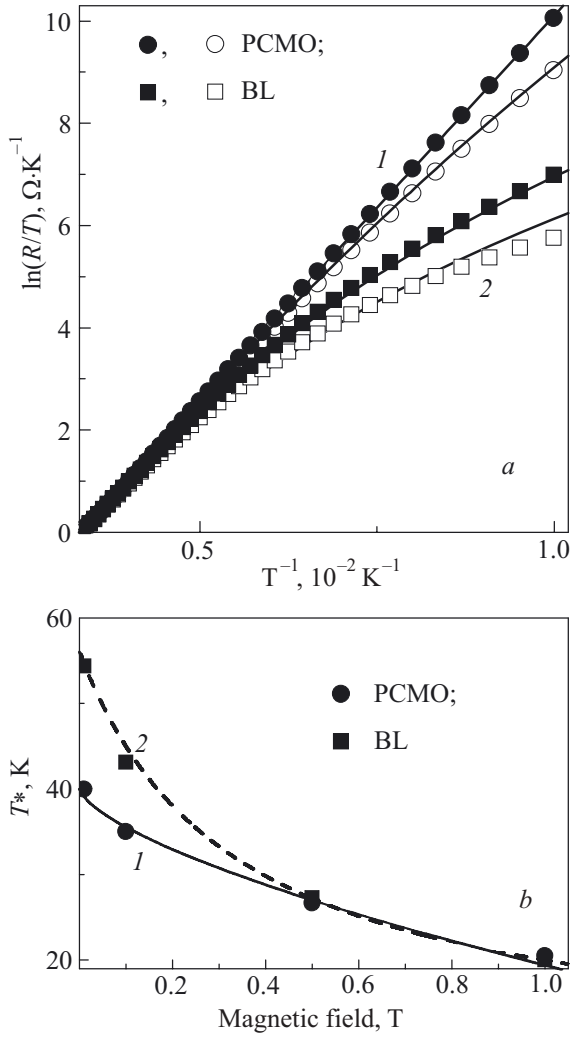


*Fig. 10.* The $\ln(R/T) - \text{vs} - T^{-1}$ plots for the PCMO film (*1*) and the PCMO/LSMO bilayer (*2*) measured without (solid symbols) and with (open symbols) an applied magnetic field. The solid lines are the corresponding theoretical curves obtained within the framework of the magnetic polaron model (*a*). The magnetic-field dependences of $T^*$ extracted from the peak in the ZFC $M(T)$ curve for the PCMO film (*1*) and the PCMO/LSMO bilayer (*2*). The solid and dashed lines are the theoretical curves obtained within the framework of the spin-glass-like and the interacting SPMs models, respectively (*b*).

A further peculiarity of the magnetic properties for the investigated films, manifesting as an additional magnetic transition at low temperature, is needed in a discussion. Figures 2 and 4 exhibit that all films exhibit the well-defined FC/ZFC $M(T)$ splitting and the non-monotonic ZFC $M(T)$ behavior with a peak at certain temperature, $T^*$. Usually such a phenomenon is interpreted as an occurrence of the cluster-glass or spin-glass-like phase, which can be governed by the microstructure peculiarities (nano-size column-like texture) [34], the doping of transition metal ions at the Mn site [35,36], the lattice strains [37], or the intrinsic phase-separation effect [13]. Two different approaches are employed for a description of the magnetic properties for manganites in the phase-separated state. There are the modified classical spin-glass theory [14,43] and the model of the superparamagnetic (SPM) clusters with a strong dipolar interaction [38–42]. Figure 10,*b* presents the magnetic-field dependences of $T^*$, which was evaluated as a peak position on the ZFC $M(T)$ curve, for

PCMO and BL. It is seen that the $T^*(H)$ dependence for the individual PCMO film can be extrapolated by the Almeida–Thouless line, predicted for a classical spin-glass [43,44]:

$$T^*(H) = T^*(0)\left[1-\left(\frac{3}{4}\frac{H^2}{J^2}\right)^{1/3}\right], \qquad (2)$$

where $J$ is the exchange integral. In spite of that the fitted $J$ value turn out to be a twice smaller than that is estimated in the framework of a mean-field model, $J = 3k_BT_C/[2zS(S+1)]$, one can consider that the agreement between the theoretical (solid line) and the experimental (circle symbols) curves is quite reasonable. Here $T_C$ = 150 K is the Curie temperature, $z$ = 6 is the number of nearest neighbor atoms (because we consider the cubic unit cell) and $S$ = 1.75 is the average spin value for the Mn ion. The observed difference in the $J$ values most probably connected with an incorrect choice of $T_C$ for the estimation of the exchange integral. In our case the Cutie point has be define the long-range order between the magnetic polarons rather than between the individual atoms. Larger distance between the nearest magnetic polarons rather than the Mn ions that can lead to a decrease of the exchange interaction. At the same time the $T^*(H)$ dependences for the PCMO sublayer more properly described by an expression, $T^*(H) = T^*(0)/(1+\beta H)$, which was obtained in the framework of model for the interacting SPM clusters [38]. Here $\beta \simeq$ 3 $T^{-1}$ is a certain coefficient between the saturation magnetic moment and an applied magnetic field. Moreover, the most significant difference between experimental $T^*(H)$ curves for the PCMO film and the PCMO sublayer observes in a low-field range. As discussed earlier at $H \to 0$ the large-size FM clusters form in the PCMO sublayer, which are induced by the FM LSMO sublayer due to a *magnetic proximity effect*. Therefore, the small-size magnetic polarons demonstrate the magnetic properties at low temperature close to the spin-glass-like system while the large-size FM clusters have magnetic behavior typical for the interacting SPM particles.

## 6. Conclusions

We have performed magnetotransport measurements of the PCMO/LSMO bilayer deposited on LAO substrate by a cross-beam laser ablation. For comparison, the PCMO and LSMO films have also been prepared. The XRD and HREM analysis reveals that the lattice parameters for the constituent sublayers in BL are very close to that for the individual films. Moreover, the tetragonal ratio, $c/a$, which defines a lattice distortion, provided by a lattice strain, is also almost the same.

It was shown that the FM transition in the LSMO sublayer at $T_C \simeq$ 325 K with the decreasing temperature significantly modifies the magnetotransport properties of the PCMO constituent sublayer, owing to an occurrence of a *magnetic proximity effect*.

(i) The cooling of the PCMO/LSMO bilayer under an applied magnetic field of 0.5 T (FC regime) leads to an appearance of the exchange bias interaction between the constituent sublayers, which is manifested by a shift of the hysteresis loop along a magnetic field axis.

(ii) The FM LSMO sublayer introduces the magnetic order into the PCMO sublayer and gives an impetus to a topological magnetic transformation (at $H \to 0$) from the small-size magnetic-polaron-PM state to the Griffiths-like phase with the large-size fluctuated FM clusters that can be treated as a localized-to-itinerant crossover in the system of polarized electrons. The fluctuated FM state, which is originated from a *magnetic proximity effect*, turn out to be a very sensitive to an applied magnetic field and can be fully frustrated at $H$ = 1 T.

(iii) A *magnetic proximity effect* manifests itself in the polaron transport as a nonlinear $\ln(R/T) - \mathrm{vs} - T^{-1}$ dependence without an applied magnetic field. It is explained by an appearance of the internal magnetic field originated from the spontaneous magnetization of the LSMO sublayer and an existence of the large-size fluctuated FM clusters.

(iiii) At low temperature the PCMO film demonstrate the magnetic properties close to the spin-glass-like system while the PCMO sublayer, owing to a *magnetic proximity effect*, has magnetic behavior typical for the interacting SPM particles.

Therefore, the development of hybrid devices based on multilayered films needs detailed information on the mutual influence between constituent layers, including the occurrence of a *magnetic proximity effect*.

This work was supported by the NRF/MEST through the Quantum Photonic Science Research Center, Korea. V. Svetchnikov is grateful to the financial support of Netherlands Institute for Metal Research.

1. M. Kiwi, *Mat. Res. Soc. Symp. Proc*. **746**, 1 (2003).
2. J. Nogués and I.K. Schuller, *J. Magn. Magn. Mater*. **192**, 203 (1999).
3. J. Nogués, J. Sort, V. Langlais, V. Skumryev, S. Suriñach, J.S. Muñoz, and M.D. Baró, *Phys. Rep*. **422**, 65 (2005).
4. K. Lenz, S. Zander, and W. Kuch, *Phys. Rev. Lett*. **98**, 237201 (2007).
5. V.G. Prokhorov, G.G. Kaminsky, V.A. Komashko, Y.P. Lee, and J.S. Park, *Fiz. Nizk. Temp*. **29**, 885 (2003) [*Low Temp. Phys*. **29**, 663 (2003)].
6. V.G. Prokhorov, V.S. Flis, G.G. Kaminsky, and Y.P. Lee, *Fiz. Nizk. Temp*. **30**, 619 (2004) [*Low Temp. Phys*. **30**, 463 (2004)].
7. Y.P. Lee, S.Y. Park, V.G. Prokhorov, V.A. Komashko, and V.L. Svetchnikov, *Appl. Phys. Lett*. **84**, 777 (2004).
8. Y.P. Lee, S.Y. Park, Y.H. Hyun, J.B. Kim, V.G. Prokhorov, V.A. Komashko, and V.L. Svetchnikov, *Phys. Rev*. **B73**, 224413 (2006).

9. V.G. Prokhorov, G.G. Kaminsky, Y.P. Lee, S.Y. Park, Y.H. Hyun, J.S. Park, V.L. Svetchnikov, *Fiz. Nizk. Temp*. **34**, 942 (2008) [*Low Temp. Phys*. **34**, 746 (2008)].
10. V.G. Prokhorov, G.G. Kaminsky, V.S. Flis, Y.P. Lee, K.W. Kim, and I.I. Kravchenko, *Physica* **B307**, 239 (2001).
11. M.C. Martin, G. Shirane, Y. Endoh, K. Hirota, Y. Morimoto, and Y. Tokura, *Phys. Rev*. **B53**, 14 285 (1996).
12. Z. Jirák, S. Krupička, Z. Šimša, M. Dlouhá, and S. Vratislav, *J. Magn. Magn. Mater*. **53**, 153 (1985).
13. For a review: see *Colossal Magnetoresistance, Charge Ordering and Related Properties of Manganese Oxides*, C.N.R. Rao and B. Raveau (eds.), World Scientific, Singapore (1998); *Colossal Magnetoresistance Oxides*, Y. Tokura (ed.), Gordon and Breach, London (1999); B. Raveau, M. Hervieu, A. Maignan, and C. Martin, *J. Mater. Chem*. **11**, 29 (2001); E. Dagotto, T. Hotta and A. Moreo, *Phys. Rep*. **344**, 1 (2001).
14. R. Rivadulla, M.A. López-Quintela, and J. Rivas, *Phys. Rev. Lett*. **93**, 167206 (2004).
15. Y.P. Lee, V.G. Prokhorov, J.Y. Rhee, K. W. Kim, G.G. Kaminsky, and V.S. Flis, *J. Phys.: Condens. Matter* **12**, L133 (2000).
16. Y.P. Lee, V.G. Prokhorov, J.Y. Rhee, and K.W. Kim, *J. Phys.: Condens. Matter* **13**, 9673 (2001).
17. A. Maniwa, K. Okano, I. Ohkubo, H. Kumigashira, M. Oshima, M. Lippmaa, M. Kawasaki, and H. Koinuma, *J. Magn. Magn. Mater*. **310**, 2237 (2007).
18. S. Schramm, J. Hoffmann and Ch. Jooss, *J. Phys.: Condens. Matter* **20**, 395231 (2008).
19. Z.Q. Yang, Y.Q. Zhang, J. Aarts, M.-Y. Wu, and H.W. Zandbergen, *Appl. Phys. Lett*. **88**, 072507 (2006).
20. S.V. Vansovskii, *Magnetism*, Nauka, Moscow (1973) [in Russian].
21. R.B. Griffiths, *Phys. Rev. Lett.* **23**, 17 (1969).
22. J.M. Ziman, *Models of Disoder*, Cambridge University Press (1979).
23. B.D. Cullity, *Introduction to Magnetic Materials*, Addison-Wesley, New York (1972).
24. J.A. Souza, J.J. Neumeier, and Y.K. Yu, *Phys. Rev*. **B78**, 014436 (2008).
25. C.M. Varma, *Phys. Rev*. **B54**, 7328 (1996).
26. A. Daoud-Aladine, J. Rodrígues-Carvajal, L. Pinsard-Gaudart, M.T. Fernández-Díaz, and A. Revcolevschi, *Phys. Rev. Lett*. **89**, 097205 (2002).
27. D. Niebieskikwiat and M.B. Salamon, *Phys Rev*. **B72**, 174422 (2005).
28. L. Wu, R.F. Klie, Y. Zhu, and Ch. Jooss, *Phys. Rev*. **B76**, 174210 (2007).
29. T. Holstein, *Ann. Phys*. (*N.Y.*) **8**, 343 (1959).
30. G. Jakob, W. Westerburg, F. Martin, and H. Adrian, *Phys. Rev*. **B58**, 14 966 (1998).
31. M. Viret, L. Ranno, and J.M.D. Coey, *Phys. Rev.* **B55**, 8067 (1997).
32. V.M. Galitski, A. Kaminski, and S.D. Sarma, *Phys. Rev. Lett*. **92**, 177203 (2004).
33. K. Steenbeck and R. Hiergeist, *Appl. Phys. Lett*. **75**, 1778 (1999).
34. V.G. Prokhorov, Y.H. Hyun, J.S. Park, J.B. Kim, G.H. Kim, Y.S. Lee, Y.P. Lee, and V.L. Svetchnikov, *J. Appl. Phys*. **104**, 103901 (2008).
35. A. Maignan, C. Martin, S. Hébert, and V. Hardy, *J. Mater. Chem*. **17**, 5023 (2007).
36. Ji-Wen Feng, C. Ye, and L.-P. Hwang, *Phys. Rev*. **B61**, 12271 (2000).
37. A. Tebano, C. Aruta, P.G. Medaglia, F. Tozzi, G. Balestrino, A.A. Sidorenko, G. Allodi, R. De Renzi, G. Ghiringhelli, C. Dallera, L. Braicovich, and N.B. Brookes, *Phys. Rev*. **B74**, 245116 (2006).
38. V.G. Prokhorov, G.G. Kaminsky, J.M. Kim, T.W. Eom, J.S. Park, Y.P. Lee, V.L. Svetchnikov, G.G. Levtchenko, A.V. Paschenko, Yu.V. Medvedev, Yu.M. Nikolaenko, G.V. Bukin, and V.A. Khokhlov, *Fiz. Nizk. Temp*. **37**, 141 (2011) [*Low. Temp. Phys*. **37**, 112 (2011)].
39. J. Du, B. Zhang, R.K. Zheng, and X.X. Zhang, *Phys. Rev.* **B75**, 014415 (2007).
40. P. Allia, M. Coisson, P. Tiberto, F. Vinai, M. Knobel, M.A. Novak, and W.C. Nunes, *Phys. Rev*. **B64**, 144420 (2001).
41. O. Margeat, M. Tran, M. Spasova, and M. Farle, *Phys. Rev*. **B75**, 134410 (2007).
42. P. Allia, F. Celegato, M. Coisson, A. Da Re, F. Ronconi, F. Spizzo, P. Tiberto, and F. Vinai, *J. Magn. Magn. Mater*. **290–291**, 580 (2005).
43. I.Ya. Korenblit and E.F. Shender, *Sov. Phys. Usp*. **32**, 139 (1989).
44. J.R.L. de Almaida and D.J. Thouless, *J. Phys*. **A11**, 983 (1978).